

# A search for the third lensed image in JVAS B1030+074

M. Zhang,<sup>1</sup> \* N. Jackson,<sup>1</sup> R. W. Porcas<sup>2</sup> and I. W. A. Browne<sup>1</sup>

<sup>1</sup>*University of Manchester, Jodrell Bank Observatory, Macclesfield, Cheshire SK11 9DL*

<sup>2</sup>*Max-Planck-Institut für Radioastronomie, Auf dem Hügel 69, D 53121, Bonn, Germany*

24 May 2018

## ABSTRACT

Central gravitational image detection is very important for the study of the mass distribution of the inner parts ( $\sim 100$  pc) of lens galaxies. However, the detection of such images is extremely rare and difficult. We present a 1.7-GHz High Sensitivity Array (HSA) observation of the double-image radio lens system B1030+074. The data are combined with archive VLBA and global-VLBI observations, and careful consideration is given to the effects of noise, CLEANing and self-calibration. An upper limit is derived for the strength of the central image of  $180 \mu\text{Jy}$  (90% confidence level), considerably greater than would have been expected on the basis of a simple analysis. This gives a lower limit of  $\sim 10^3$  for the ratio of the brightest image to the central image. For cusped models of lens mass distributions, we have made use of this non-detection to constrain the relation between inner power-law slope  $\beta$  of the lensing galaxy mass profile, and its break radius  $r_b$ . For  $r_b > 130$  pc the power-law slope is required to be close to isothermal ( $\beta > 1.8$ ). A flatter inner slope is allowed if a massive black hole is present at the centre of the lensing galaxy, but the effect of the black hole is small unless it is  $\sim 10$  times more massive than that implied by the relation between black hole mass and stellar velocity dispersion. By comparing four epochs of VLBI observations, we also detected possible superluminal motion in the jet in the brighter A image. The B jet remains unresolved, as expected from a simple lens model of the system.

**Key words:** galaxies: structure - galaxies: individual: B1030+074 - gravitational lensing

## 1 INTRODUCTION

Gravitational lensing is an important method to probe the mass distribution in the Universe, from the largest scales down to sub-galactic scales. The matter in our universe is thought to be predominantly non-baryonic, consisting of a weakly-interacting form known as Cold Dark Matter (CDM). CDM simulations have so far been very successful in reproducing large-scale structures observed in large galaxy surveys such as the 2dF (Colless et al. 2001; Peacock 2003) and SDSS (Doroshkevich et al. 2004). CDM structures form potential wells, and numerical simulations predict that these have a characteristic radial mass profile consisting of a broken power law with a flatter central slope, now known as a NFW profile (Navarro, Frenk, & White 1996, 1997). Baryons dominate the central regions of galaxies, having cooled into the centres of the potential wells formed by the CDM (Rees & Ostriker 1977; Navarro & Benz 1991; Combes 2004). However, the detailed physics is difficult;

firstly, large-scale CDM simulations reach the limit of their current resolution on scales of  $\sim$  kpc (e.g. Ghigna et al. 2000; Sommer-Larsen et al. 2003; Robertson et al. 2004; Kang et al. 2005) and second, the baryon content requires the input of detailed micro-physics (e.g. White & Frenk 1991; Gnedin et al. 2004; Macciò et al. 2006).

In the central regions of galaxies we have reasons to believe that an additional component is present, namely a massive black hole. At the centre of our own Galaxy there is strong evidence for the existence of a  $3.7 \times 10^6 M_\odot$  black hole (Ghez et al. 2005), and more massive black holes of  $\sim 0.002$  times the total galaxy mass have been inferred from kinematical observations (Lauer et al. 1997). Some galaxies have black hole masses as large as  $1 \times 10^9 M_\odot$  (Kormendy et al. 1996). Radio observations have also shown that massive black holes exist in active disk galaxies (Miyoshi et al. 1995). The black hole mass is also found to scale with the stellar velocity dispersion of the bulge (Ferrarese & Merritt 2000; Gebhardt et al. 2000; Tremaine et al. 2002), in a process which is probably

\* E-mail: mzhang@jb.man.ac.uk

related to galaxy formation in a way that is not yet completely understood.

The mass distribution in the central regions of galaxies can be probed by gravitational lensing, as was first pointed out by Wallington & Narayan (1993). This is because the central image of a gravitational lens system passes through the centre of the lens galaxy potential, and its magnification can in principle tell us about the nature of the potential within  $\sim 100$  pc from the centre of the galaxy. In general, the more nearly singular the potential, the more strongly demagnified is the central image.

A number of theoretical and observational analyses of central images of galaxy lens systems have been carried out to date. A strict proof for the general theorem that lenses have odd numbers of images was carried out with Lorentzian manifolds (McKenzie 1985), though its applicable conditions are arguably not universal (Gottlieb 1994). However, most physical models show the existence of the central odd image (Section 4). Observationally, there are some cases in which radio emission is detected near the centre of a lens galaxy, for example in the radio-loud lens systems MG J1131+0456 (Chen & Hewitt 1993), QSO 0957+561 (Harvanek et al. 1997), CLASS B2045+265 (Fassnacht et al. 1999) and CLASS B2108+213 (McKean et al. 2005). None of these are secure or even probable detections of a central lensed image, as the central component is quite likely to be due to radio emission from active nuclei in the lens galaxies. The lens system PMN J1632–0033 has yielded the most likely detection of a central image, although in this case free-free absorption in the lensing galaxy is required to modify the radio spectral index of the central image to make it agree with that of the other images (Winn et al. 2003, 2004b). In addition, there is one optically-selected three-image case, APM 08279+5255 (Ibata et al. 1999; Egami et al. 2000; Muñoz et al. 2001), which may also be caused by a “naked cusp” configuration rather than a central minimum (Lewis et al. 2002). A likely central fifth image has recently been discovered in SDSS J1004+4112 in which the lens is a cluster of galaxies (Inada et al. 2005). Recently the more systematic Extragalactic Lens VLBI Imaging Survey (ELVIS) project has attempted to find detections or limits on core images, resulting in one non-detection so far in PMN J1838-3427 (Boyce et al. 2006).

There are different views on the mass distribution in the inner regions of galaxies. Existing observations can be used to constrain the mass distribution of central regions of the lensing galaxy. Since numerical simulations predict double power-law models with central cusps rather than core radii (Navarro et al. 1997), and the observed light distributions seem also to follow cusp-like laws in the centres of nearby early-type galaxies (Faber et al. 1997), these analytic forms are usually assumed when fitting central mass distributions (Muñoz et al. 2001; Rusin et al. 2003). On the other hand, in some cases, in particular in low-surface-brightness galaxies where a large dark matter component may be present, de Blok et al. (2001) have argued that the central power-law exponent is close to flat, corresponding to a central density “core”. Central image detection (or limits) can help us to understand the mass distribution.

A thorough analysis of the available constraints from the non-detection of the central image has been carried out by Keeton (2003) and Mao et al. (2001) have extended the

analysis to cover the properties of central black holes. In principle, a non-detection of a central image implies either a relatively steep inner mass slope or a small break radius in the power-law. Rusin & Ma (2001), based on analysis of six systems, found that the inner mass slope index is unlikely to be flatter than 0.8. Keeton (2003) discussed a range of models for realistic lens galaxies and found that galaxies which yield central image magnifications of  $\mu \sim 0.001$  are likely to be the most common, and that in 10–20% of cases a central black hole may be large enough, and positioned close enough to the central image, to demagnify it into invisibility.

In this paper we consider the lens system B1030+074 (Xanthopoulos et al. 1998). This is in many ways the ideal system in which to look for an odd image. First, it is very strong, having a primary component with flux density of more than 200 mJy at 5 GHz (Xanthopoulos et al. 1998). Second, being a radio source, the detection of the central image is made easier by the absence of strong radio emission from the lensing galaxy. Third, it has two observed images which are relatively asymmetric in flux density ( $\sim 15 : 1$ ). Such lens systems are likely to give rise to central images which are less strongly demagnified than four-image lens systems or more symmetric two-image systems (Winn et al. 2003). Our aim was to produce an image with an rms noise of about  $10^{-4}$  of the flux of the primary, and hence give us a reasonable chance to detect the central image based on the prediction of Keeton (2003). In the following Section 2, 3, 4 and 5, we present results from observations, a derivation of the upper limit to detection, results from lens modelling and detection of superluminal jet motions, respectively.

## 2 OBSERVATIONS

The double-image lens system B1030+074 was discovered during the 8.4-GHz Jodrell-VLA Astrometric Survey (JVAS) in 1992 (Browne et al. 1998; Xanthopoulos et al. 1998). A follow-up 1.7-GHz observation with Very Long Baseline Array (VLBA) and Effelsberg showed the primary image had a flux density of 250 mJy and the secondary image had a flux density of 17.4 mJy with a separation of 1.567 arcsec at a position angle of  $143^\circ.4$ . The nominal dynamic range of the 1.7-GHz map was about 6000:1 (Xanthopoulos et al. 2001). We have made a new L-band Very Long Baseline Interferometry (VLBI) observation with the High Sensitivity Array (HSA: VLBA, VLA, Green Bank Telescope and Arecibo) aimed at approaching a higher dynamic range in order to detect any central image or improve the upper limit. This 1.7-GHz dual polarisation observation was carried out on 2004 December 27. About 3 hours integration were obtained with an aggregate bit rate of  $256 \text{ Mbs}^{-1}$ . In frequency this corresponds to 4 IFs each containing 32 channels of 0.25 MHz, using 2 bits/sample. The data were correlated using the VLBA correlator in Socorro, averaged into 2-s bins. A single field centre was used, centred on the mid point between image A and B.

The data calibration was mainly carried out with AIPS<sup>1</sup>. Bad data were flagged, including the removal of the upper

<sup>1</sup> the Astronomical Image Processing System distributed by NRAO (National Radio Astronomy Observatory)

two spectral channels, all baselines involving the Mauna Kea VLBA antenna, and a large segment of data from the Green Bank antenna in the first hour of observations. The VLBA calibration transfer, written by the correlator into the data file, was applied, having been corrected for an incorrect system temperature due to a VLA mode single dish/phased array recognition problem (Sjouwerman 2005, NRAO communication). The data were re-inspected and further sporadic episodes of bad data were flagged. A fringe-fit was then performed using the data on the target source B1030+074; we have experimented with use of a two-component model and a point source in the fringe fit and find that little difference is evident. The data after fringe fitting were checked to ensure a flat response across the bandpass, and the phase and amplitude solutions derived during the calibration process were applied to the data.

The data were averaged in time using the AIPS task UBAVG, which performs a baseline-dependent time averaging, giving  $< 1\%$  flux reduction by time-average smearing over the 1600-mas extent of the source. In frequency, the data were then averaged into 8 channels, each with a bandwidth of 1 MHz, which gives a flux reduction of  $< 3\%$  over the required field of view. Images were produced using the AIPS IMAGR program, which implements the Clark version of the CLEAN algorithm (Högbom 1974; Clark 1980). The data were self-calibrated using the initial image as a model, taking CLEAN components up to the first negative. A global amplitude self-calibration was first applied, using a very long solution interval to adjust the flux scale of the antennas to each other. After production of a new CLEANed image, a phase self-calibration was then applied using a short solution interval. After correction of phases in this way, a further round of self-calibration using amplitudes and phases was performed, with a solution interval of 15 minutes. No further improvement was observed in the maps by use of further self-calibration. Final images were produced using *uv* grid weighting close to uniform and weighting of the data points by the statistical weight appropriate to the size of the telescopes on the baseline involved. Natural grid weighting in principle should give better signal-to-noise by a factor of  $\sim 2$ , but was found to give very poor results in practice. This is because calibration errors and CLEAN errors are more important in high-dynamic-range mapping, we cannot expect the thermal noise limit to apply. In general, for producing the final image from the self-calibrated data we CLEANed the whole image, or a large part of it, using a large number ( $\sim 20000$ ) of CLEAN iterations, a procedure which we justify in detail in Section 3. Gaussian model fitting to the final images was done with the AIPS task JMFIT in the image plane.

To get the maximum dynamic range, we also obtained data on B1030+074 from previous 1.7-GHz VLBI observations (1998 BX003, 2000 GX006, 2001 GX007), and combined them with our new observation (2004 BJ054). Data from the previous epochs were calibrated and imaged in the same way as previously described. For each epoch, CLEANed maps were made individually, and combined together in the map plane weighting by  $1/\sigma^2$ , where  $\sigma$  is the measured rms noise in each image. Our combined global-VLBI + HSA map of B1030+074 made with a restoring beam of  $7.7 \times 4.5 \text{ mas}^2$  at a position angle of  $-10^\circ.85$ , is shown in Fig. 1, together

with enlarged versions of images A and B. Parameter values from model fitting are given in Table 2.

Image A is resolved with an extended jet that can be seen in the north-east direction having a length of about 20 mas, while image B is not resolved. A super-resolved image with a half-size restoring beam (i.e.,  $3.8 \times 4.5 \text{ mas}^2$ ) was made, but the B jet was still not detected. The whole field CLEAN of the HSA map gives a noise level of  $\sigma \sim 24.1 \mu\text{Jy beam}^{-1}$  around the expected position of the central image (see Table 1). After the combination of the maps from four epochs, the noise level is reduced to  $\sigma \sim 19.9 \mu\text{Jy beam}^{-1}$ . The dynamic range achieved in the final map is more than 10000:1 ( $S_A/\sigma > 10000$ , see Table 2).

To locate the lens galaxy and hence derive the likely position of the central image, we used the HST WFPC2 I-band image (Fig. 2) of B1030+074 (Xanthopoulos et al. 1998) from the HST archive to measure the position of the lens galaxy. We can clearly see both the lensed images and the lens galaxy which has an extended structure to the west. The separation from lens galaxy G to the B image is  $127 \pm 10$  mas in position angle  $149^\circ.7 \pm 4^\circ.0$  from north through east; there is no obvious detection of a radio source above the local noise level at the position of G.

The flux density of both A and B components has varied ( $\sim 10\%$ ) over the seven-year span of observations. Variation was also seen in a monitoring campaign reported by Xanthopoulos et al. (2000) which consisted of 47 epochs of VLA observations spread over 240 days. Both datasets are not inconsistent with intrinsic variation of the source, together with an expected time delay of  $\sim 100\text{--}150$  days predicted by simple lens models. In the case of J1838–3427, Winn et al. (2004a) deduce that Galactic scintillation makes a major contribution to the variability; this process is less likely to operate in B1030+074 due to the relatively high ( $b = 52^\circ$ ) Galactic latitude.

### 3 DERIVATION OF THE UPPER LIMIT

The  $3\text{-}\sigma$  limit of our final HSA map is about  $70 \mu\text{Jy beam}^{-1}$ , and this level has traditionally been regarded as the effective upper limit on the central-image flux density if there is no obvious detection. This is not the case, for two reasons. First, the image has undergone a CLEANing and self-calibration process, which may have removed flux from any central image. Second, the uncertainty in the position of the central image means that the image statistics must be considered carefully. We consider each issue in turn.

#### 3.1 CLEANing and self-calibration effects

The use of the CLEAN algorithm in the mapping procedure may result in elimination of faint images of a few  $\sigma$ , a problem known as ‘‘CLEAN bias’’ (Condon et al. 1998). Simulations with artificial sources show that sources up to  $6\sigma$  may be eliminated in this way if excessively CLEANed, but that use of CLEAN boxes around the true source position should allow them to be recovered. It is also possible that the use of self-calibration may lead to the adjustment of the data in such a way as to eliminate weak sources, by partially absorbing them into the calculated gains for each telescope.

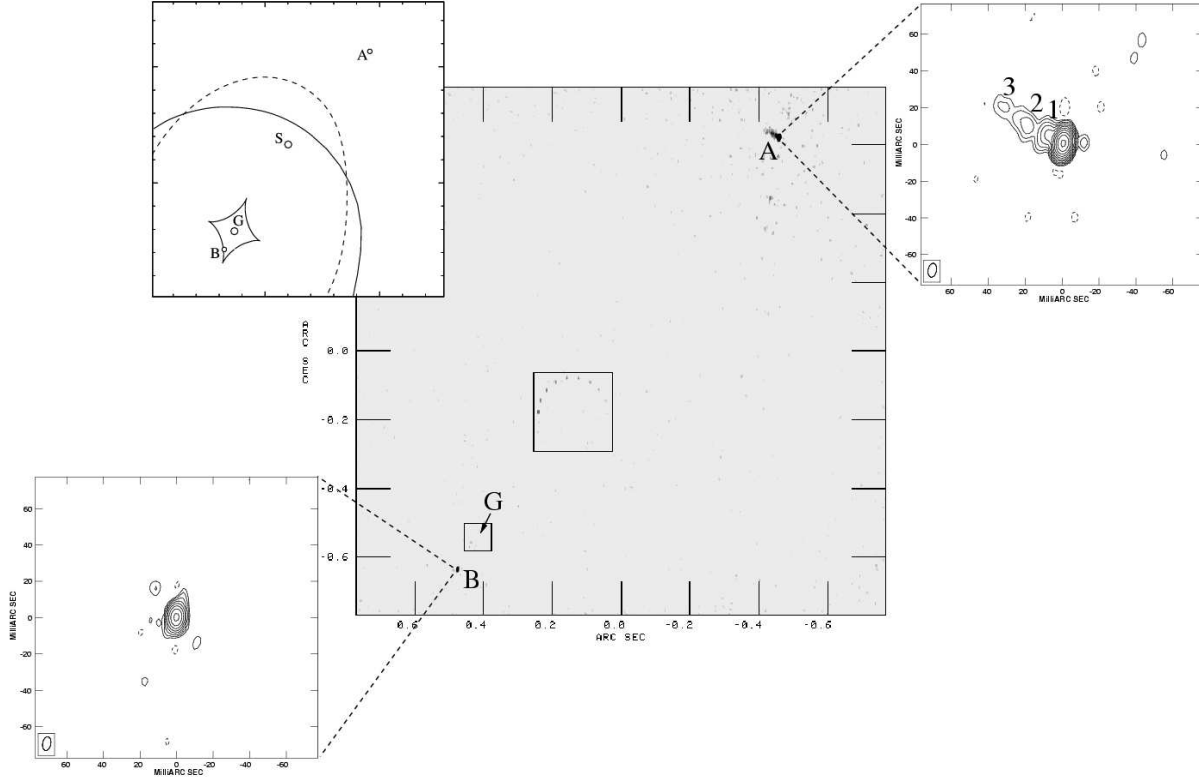


**Figure 1.** Combined global-VLBI + HSA images of B1030+074. The restoring beam size is  $7.7 \times 4.5 \text{ mas}^2$  at a position angle of  $-10^\circ.9$ . Labels A, B, G and S denote primary A, secondary B images, lens galaxy and the source respectively. Image A and image B are shown in two separate magnified figures. Contours in the maps are plotted at multiples  $(-1, 1, 2, 4, 8, 16, 32, 64, 128, 256, 512, 1024, 2048) \times 3\sigma$  where  $\sigma$  is the off-source local rms noise in the map ( $53 \mu\text{Jy beam}^{-1}$  in A image and  $26 \mu\text{Jy beam}^{-1}$  in B image). The top-left figure shows a fitted SIE model, while the solid curves are caustics and the dashed one is the critical curve. The two boxes in the map are our CLEAN recovery test region and third image prediction region respectively, see details in Section 3.

Experiment code	Telescope	Observing date (yyyy mm dd)	Time on source (min)	Measured rms noise ( $\mu\text{Jy beam}^{-1}$ )	Thermal noise ( $\mu\text{Jy beam}^{-1}$ )
BX003	VLBA+Eb	1998 06 10	705.00	61.8	44.4
GX006	VLBA+Eb+Jb+Wb	2000 02 12	545.00	58.1	24.1
GX007	VLBA+VLA+EVN subset	2001 02 09	526.00	39.5	18.9
BJ054	HSA	2004 12 27	166.25	24.1	8.2

**Table 1.** Noise levels in the central image regions of four epoch 1.7-GHz VLBI/HSA observations

	R.A. offset (mas)	Dec offset (mas)	Flux density (mJy)	Peak intensity ( $\text{mJy beam}^{-1}$ )
A	0.0000	0.0000	$258 \pm 13$	$208 \pm 10$
A1	$5.613 \pm 0.006$	$3.158 \pm 0.005$	$8.5 \pm 0.4$	$3.6 \pm 0.2$
A2	$20.47 \pm 0.03$	$9.96 \pm 0.04$	$2.6 \pm 0.1$	$0.73 \pm 0.04$
A3	$30.0 \pm 0.1$	$17.4 \pm 0.1$	$1.00 \pm 0.05$	$0.24 \pm 0.01$
B	$934.987 \pm 0.001$	$-1258.092 \pm 0.002$	$16.9 \pm 0.8$	$12.5 \pm 0.6$
G	$869.0 \pm 10.0$	$-1147.0 \pm 10.0$	-	-

**Table 2.** The observational constraints from combined VLBI + HSA images. A1, A2 and A3 are jet components within component A (top-right figure in Fig. 1) and G is the lensing galaxy. The position of G comes from HST I-band image (see text).

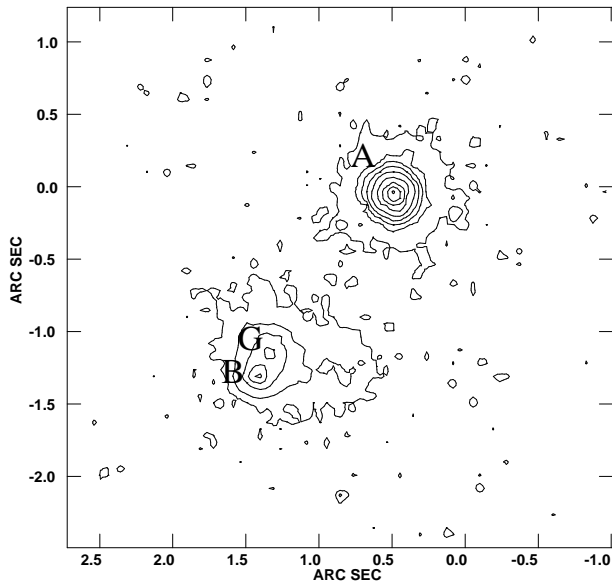


**Figure 2.** HST I-band image of B1030+074. The diffuse double-peak pattern at the lower part includes the B image and lens galaxy. Contours in the map are plotted at multiples  $(-1, 1, 2, 4, 8, 16, 32, 64, 128, 256, 512) \times 0.35\%$  peak value. The two images and lens galaxy are labelled as A, B and G respectively.

In order to assess this problem, we have used the AIPS task UVMOD to add artificial point sources with a range of fluxes to the calibrated  $uv$  data, and determined whether they are recovered during passage through our self-calibration and mapping procedure. 18 artificial point sources were used simultaneously, arranged in a ring of diameter 200 mas (see Fig. 3) and with flux densities ranging from  $60 \mu\text{Jy}$  to  $1 \text{ mJy}$ . This also allowed us the opportunity to adjust the procedure in order to recover the weakest possible source. The philosophy throughout the process has been to apply the same procedure to the artificial images as to the possible central image.

For reasons which we have been unable to determine, the use of relatively tight CLEAN boxes around components A and B gives poor noise characteristics and a high rms in the rest of the image, including the position of the possible central image. On the other hand, CLEANING the whole image gives the low noise ( $24 \mu\text{Jy beam}^{-1}$ ) seen in Fig. 1 but relatively poor recovery of the artificial images. An alternative boxing scheme is to CLEAN the majority of the image, leaving a gap around the ring of artificial sources and the position of the central image, but in addition including a small box of  $10 \times 10 \text{ mas}^2$  around the expected position of each individual artificial image and of the central image. This gives good results in that artificial sources of  $100 \mu\text{Jy}$  can be recovered; because the artificial sources and any potential central image are treated identically, we can be confident that any real central image at this flux density level could be detected.

The results are shown in Figs. 3 and 4. The best recovery is from our HSA data, with recovery of  $100 \mu\text{Jy}$  sources. However, in the previous three VLBI observations, stronger sources than this (up to  $200 \mu\text{Jy}$ ) were in many cases not recovered. In both cases, the recovery of artificial test sources is only achieved at between 5 to 10 times the expected thermal noise. In addition, our procedure does not recover the

full flux density of the artificial sources. In Fig. 4 we plot the flux density inserted against the flux density recovered. Although there is considerable scatter in the relation, a linear fit gives a gradient of 0.72, implying a  $\sim 30\%$  reduction in flux density caused by the self-calibration and mapping process.

One possibility is that the weighting of the individual antennas could be responsible for the non-recovery of weak sources, since the HSA is a combination of ten small antennas and three (Green Bank Telescope, the phased VLA and Arecibo) which have orders of magnitude greater collecting area. If the large telescopes are given their full statistical weight, the number of constraints used to derive the amplitude and phase corrections applied by self-calibration is effectively reduced, because few baselines are weighted significantly and in fact the signal is dominated by three highly sensitive baselines. This in turn means that the solution for the amplitude and phase errors on the large telescopes is under-constrained, and allows genuine structure to be removed by the corrections. To test this possibility, we weighted down the large telescopes, up to the extreme case of treating all telescopes with equal weight, at a cost of an increase in the thermal noise. However, we did not find much improvement of the recovery of the added sources, and in fact most added sources suffered worse flux loss.

### 3.2 Statistics of non-detections

We will take a simple and conservative approach to assessing the detectability of a third image in our data. We would like to be able to give a value for probability that we would have detected a third image of flux density  $\geq S$  in our data, if it were there. Unfortunately we cannot do this. We can assess the probability of detecting a source of flux density  $S$  by doing simulations but not the cumulative probability of detecting an image  $\geq S$ . This is because we do not know the expected distribution of the third image flux densities over which we should integrate. However, one thing we can be confident of is that the detectability of images increases with increasing flux density. This means that, if we assess the probability  $P^*$  of detecting images of flux density  $S$  by adding artificial sources of this flux density to our observed data, and see how many we recover, the result can give us a lower limit on the desired cumulative probability. We will adopt  $P^* = 0.9$  as our conservative limit on the probability of detecting an image, if it had a strength of  $\geq S$ . We now describe how we search the dataset before we return to the probability calculation.

Because of uncertainties in the galaxy position, and because the third-image position depends on the adoption of a model, we have to consider the pixel values in the final map over a search box rather than at a single position.

Defining the search box depends on the adoption of a model. We defer detailed discussion of this model to the next section, but note that its two principal free parameters are the break radius  $r_b$  and inner power-law slope  $\beta$  of the galaxy mass distribution. Fig. 5 shows the parameter space explored to find possible positions of the central image, and the predicted third image positions are shown in Fig. 6. From Fig. 6, we found that all the possible third image positions are enclosed in a club-shaped pattern along the major axis

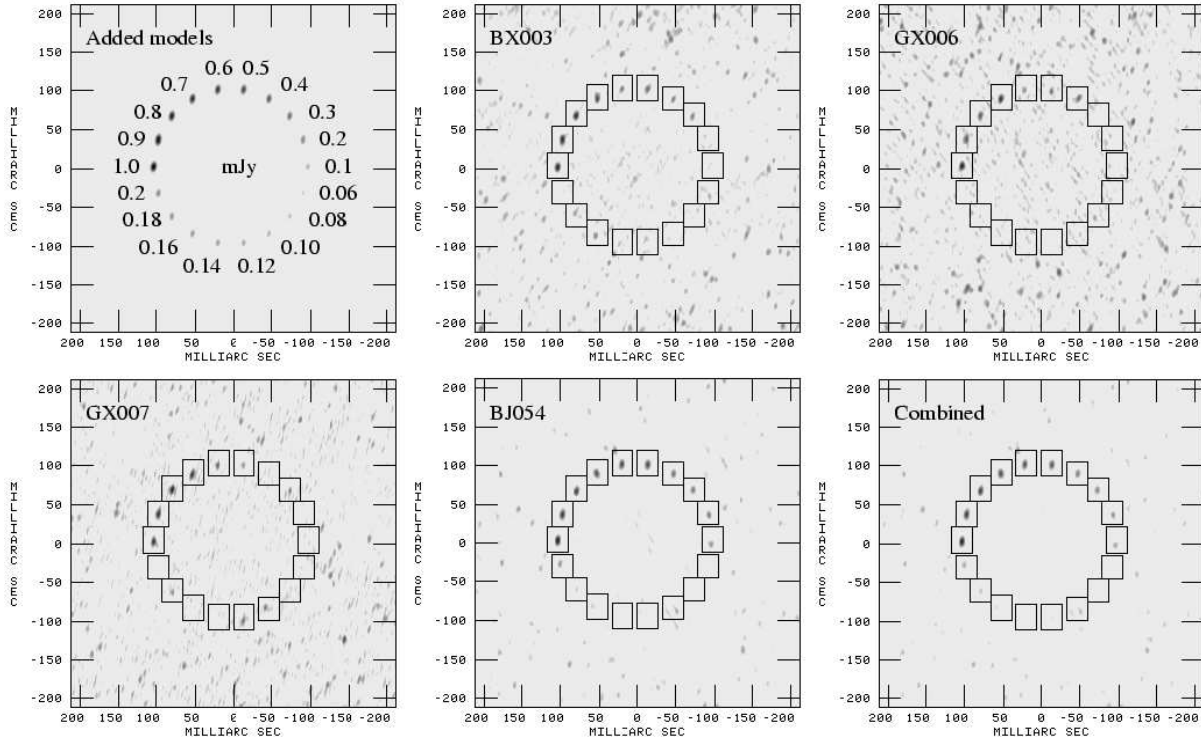


**Figure 3.** Artificial source ‘ring’ recovery test. The solid rectangles are used as a guide to the source positions. The positions of our 18 added models in the  $uv$  data form a circle with  $20^\circ$  separation from each other. The upper half-circle includes 10 sources from  $1000 \mu\text{Jy}$  to  $100 \mu\text{Jy}$  in steps of  $100 \mu\text{Jy}$ , and the lower half-circle includes 8 sources from  $200 \mu\text{Jy}$  to  $60 \mu\text{Jy}$  in steps of  $20 \mu\text{Jy}$ . For comparison, all maps are set to linear scale with a flux density range of from  $0.03 \text{ mJy}$  to  $1 \text{ mJy}$ .

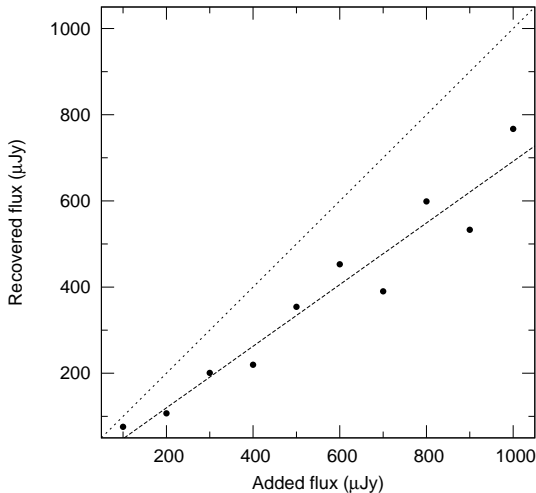


**Figure 4.** Flux loss in the HSA map from our mapping procedure, expressed in a plot of the flux density of an artificially added source against the recovered flux density. The dashed line is a linear fit to the data which has a slope of 0.72. The dotted diagonal line has a slope of 1.

of the elliptical mass distribution. The area of the club shape is about  $840 \text{ mas}^2$ , i.e., of about 24 beams.

Using  $10 \times 10 \text{ mas}^2$  CLEAN boxes in this area for imaging, as described in the previous subsection, gives a maximum flux density within this region of  $42 \mu\text{Jy}$ . This value is consistent with being a noise spike, and in fact if the noise

were Gaussian (which it is not) one would expect several such values within the  $840\text{-mas}^2$  search box.

We now return to the probability calculation. We recover no source stronger than  $42 \mu\text{Jy}$  from the search box. What is the flux density,  $S$ , that an image would have to have for  $P^* = 0.9$ ? To find this we have experimented with artificial sources of different flux densities and find that using sources of  $180 \mu\text{Jy}$ , 90% of them are recovered with flux densities greater than  $42 \mu\text{Jy}$ . Therefore our conclusion is that the probability of detecting an image using our search technique is  $\geq 90\%$ , provided its flux density is  $\geq 180 \mu\text{Jy}$ . A more detailed interpretation of this upper limit is given in Appendix A.

#### 4 LENS MODELLING

The mass distribution of galaxies has been a subject of debate in the last two decades. On the scale of the outer images in lens systems (normally a few kiloparsecs) an isothermal profile is usually a good fit (e.g. Koopmans et al. 2006). In the past, power-law models with a nearly isothermal profile and a central flat core were used (e.g. Lauer 1985). However, numerical simulations (Navarro et al. 1997) and HST observations (Faber et al. 1997) have been used to argue for a more general description in which galaxies have a two-power-law form with a central cusp. Normally, for a weak cusped model, the odd number theorem applies and a third image exists (Evans & Wilkinson 1998).

We adopt a typical spherical density profile of a cusped

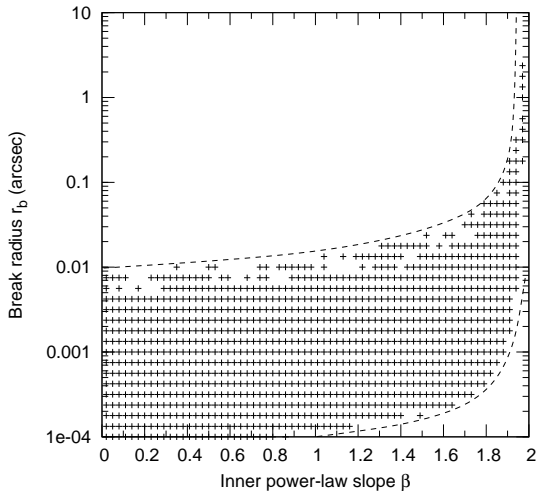


**Figure 5.** Grid-search sampling in  $\beta - r_b$  plane. The ‘+’ symbol denotes the grid points we sampled to determine the predicted central image position. Above the dotted line, the central image is predicted at a level which would be obvious from inspection of the radio map.

model (e.g. Muñoz et al. 2001):

$$\rho(r) = \frac{\rho_0}{(r/r_b)^\beta [1 + (r/r_b)^2]^{(\eta-\beta)/2}} \quad (1)$$

where  $\rho$  is the mass density,  $\rho_0$  is the scale factor,  $r$  is the radius,  $\eta$  is the outer slope,  $\beta$  is the inner slope, and  $r_b$  is the break radius. This two power-law distribution degenerates to single power-law distributions  $r^{-\eta}$  or  $r^{-\beta}$  respectively when  $r \gg r_b$  or  $r \ll r_b$ . In the limit  $\beta \rightarrow 0$ , we have a cored model, whereas in the limit  $\beta = \eta = 2.0$ , we recover a singular isothermal model (SIE). More generally, for the ellipsoidal models, the  $r$  should be replaced by triaxial coordinates ( $r^2 = x^2/a^2 + y^2/b^2 + z^2/c^2$ ) (Chae et al. 1998).

Numerous authors have pointed out that regions of the  $r_b - \beta$  parameter space can be ruled out by the non-detection of central images in gravitational lens systems. In all cases a power-law model with an isothermal slope or steeper causes infinite demagnification of the central image. Early studies by Wallington & Narayan (1993) examined softened power-law models with a core; in this case an upper limit on the core radius could be derived. Evans & Hunter (2002) developed a general formalism for cored profiles and found that for observed systems with missing central images, the typical core radius of the lensing galaxy must be  $< 300$  pc; they concluded that the mass profile must be nearly cusped and that the cusp must be isothermal or stronger. Rusin & Ma (2001) used the non-detection of central images in a number of Cosmic Lens All-Sky Survey (CLASS) (Myers et al. 2003; Browne et al. 2003) gravitational lens systems to infer limits on single power-law models (in which  $\beta = \eta$  and  $r_b$  is therefore irrelevant) and for B1030+074 found that the then existing limit on the central image implied a central power law slope  $\beta > 1.91$ . Muñoz et al. (2001), Winn et al. (2003, 2004a) and Boyce et al. (2006) explicitly studied the allowed region of the  $r_b - \beta$  plane for various lens systems, assuming an isothermal outer slope ( $\eta=2$ ). In each case the non-detection of a central image allows the exclusion of a region of this plane with a relatively flat inner slope (low  $\beta$ ) and large break radius (high  $r_b$ ), and this restriction be-

comes more powerful as the limit on the ratio between the central image and the brightest image becomes more stringent. In the case of a detection (Winn et al. 2004b) an allowed locus on this plane can be inferred.

The number of degrees of freedom in a simple cusp model is negative, since the free parameters (dimensionless surface density  $\kappa_0$ , ellipticity  $e$ , position angle  $\theta$ ,  $r_b$ ,  $\beta$ , source and galaxy  $(x, y)$  positions) outnumber the measured parameters (e.g. Boyce et al. 2006). Following Winn et al. (2003) and Boyce et al. (2006), we therefore investigated the behaviour of cusped models for B1030+074 with different values of inner power-law slope,  $\beta$ , and break radius,  $r_b$ , together with a fixed isothermal outer power-law slope  $\eta = 2$ . This was repeated for different flux ratios between the primary image A and the third image C (see Fig. 7). We used the fast Fourier expansion method of Chae et al. (1998) and Chae (2002) for this purpose. The higher the observational limit on the magnification ratio, the larger the non-detection region above the solid lines. For our value of  $S_A/S_C \sim 1000$  (from our derived upper limit on  $S_C$ ) and  $r_b \gtrsim 130$  pc, we obtain an inner power-law slope  $\beta$  greater than 1.8.

One possibility is that a massive central black hole in the lens galaxy could suppress the central image (Mao et al. 2001; Keeton 2001, 2003). Keeton (2003) analysed the likely suppression of central images for different black hole masses and concluded that the average degree of suppression is quite small; the exception is in those cases where the central image is extremely faint in any case. Rusin & Ma (2001) calculate explicitly the case of B1030+074, using a single power-law model ( $\beta = \eta$ ) together with a plausible black hole mass, and conclude that the limit on the power-law slope needs to be relaxed from  $\beta > 1.91$  to  $\beta > 1.83$ .

A plausible black hole mass can be estimated by using the empirical correlation between the central black hole mass and the galactic bulge velocity dispersion (Ferrarese & Merritt 2000; Gebhardt et al. 2000; Tremaine et al. 2002)

$$\log(M_{BH}/M_\odot) = \alpha + \beta \log(\sigma/\sigma_0), \quad (2)$$

where  $\beta = 4.02 \pm 0.32$ ,  $\alpha = 8.13 \pm 0.06$ ,  $\sigma_0 = 200 \text{ km s}^{-1}$  are the fitted values from Tremaine et al. (2002). Since the galactic mass distribution is very close to isothermal, we can use the relation

$$\Delta\theta/2 = 4\pi(\sigma^2/c^2)(D_{ds}/D_s) \quad (3)$$

to estimate the velocity dispersion of the lens galaxy, where  $\Delta\theta$  is the angular separation between image A and B,  $D_{ds}$  and  $D_s$  are the angular diameter distances between lens and source, and source and observer, respectively. For the case of B1030+074,  $\Delta\theta \simeq 1.567$  arcsec, which gives a velocity dispersion  $\sigma$  of  $233 \text{ km s}^{-1}$ , and hence a central black hole mass  $M_{BH}$  of about  $2.5 \times 10^8 M_\odot$ <sup>2</sup>. Applying the cusped model together with this black hole mass, we can get the modified relation between break radius  $r_b$  and inner power-law slope  $\beta$ , which is shown in Fig. 7. In the limit of large break radius ( $r_b \rightarrow \infty$ ), the cusped model approaches a single power-law model similar to the simulation of Rusin & Ma (2001) previously described. In our model, the asymptotic value of inner

<sup>2</sup> Here and elsewhere in this paper we use a flat  $\Lambda$ CDM cosmological model with  $\Omega_m = 0.3$ ,  $\Omega_\Lambda = 0.7$  and  $H_0 = 72 \text{ km s}^{-1} \text{ Mpc}^{-1}$ .

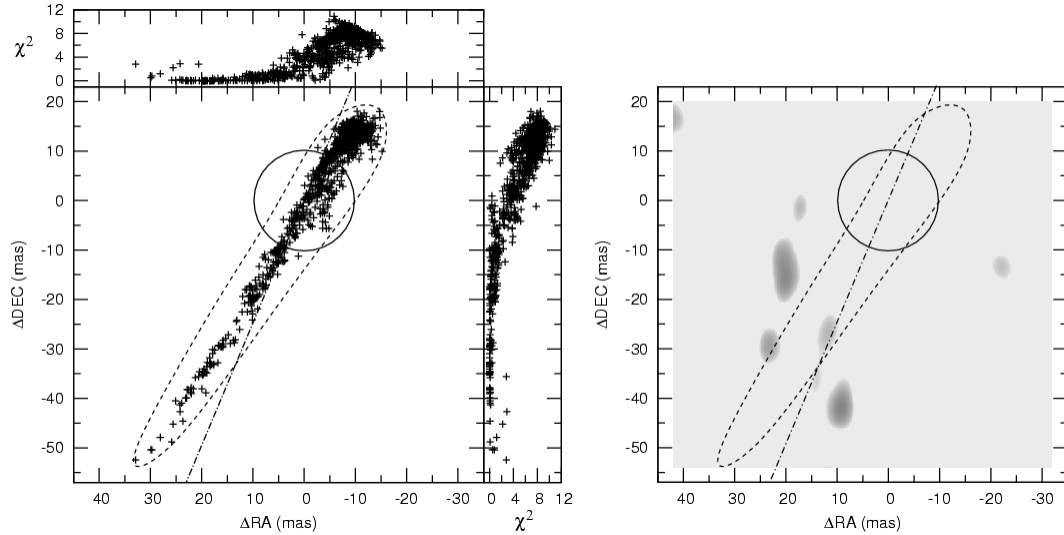


**Figure 6.** Predicted third image positions from cusped models. The solid circle is the galaxy position with  $1\sigma$  error. The dot-dashed line denotes the major axis of the elliptical mass distribution. In the left figure, the ‘+’ symbols denote the predicted third image positions in the image plane from each fit using different values of  $r_b$  and  $\beta$ . The club-shaped dashed line pattern encloses all the predicted third image positions in our test and has an area of  $840 \text{ mas}^2$ ; the top and right panels show the  $\chi^2$  distributions of each fit, as a function of  $\Delta\text{RA}$  and  $\Delta\text{DEC}$  respectively. In the right figure, we show the HSA map of the predicted third image region overlapped with the club pattern, and the rms uncertainty of the galaxy position as a circle. In these models, the galaxy position has been allowed to vary, but with a Gaussian penalty function based on our knowledge of its position from the HST image and the rms uncertainty.

power-law slope  $\beta \simeq 1.95$ , and  $\beta \simeq 1.91$  with a  $2.5 \times 10^8 M_\odot$  central black hole in the lensing galaxy. If we cut off the break radius at the Einstein radius of an isothermal model, we get an inner power-law slope  $\beta \simeq 1.93$ , and  $\beta \simeq 1.88$  with a  $2.5 \times 10^8 M_\odot$  central black hole. Obviously, a central massive black hole affects the  $r_b - \beta$  curve more when the flux ratio  $S_A/S_C$  is bigger. The  $2.5 \times 10^8 M_\odot$  black hole derived from the  $M_{BH} - \sigma$  relation does not soften the cusped mass profile significantly. We would need to add a black hole of 10 times greater mass in order for the cusped mass profile to be significantly shallower for the same  $S_A/S_C$  constraint. This result agrees well with Keeton’s conclusion from simulations of star+halo CDM mass models, that black holes would have to lie off the  $M_{BH} \sim \sigma$  relation by at least a factor of 10 in mass to significantly affect the central images (Keeton 2001).

## 5 SUPERLUMINAL JET?

The jet within the A component is potentially useful astrophysically. First, because of the stretching induced by lensing magnification, any superluminal motion is easier to observe. Superluminal motion was predicted four decades ago (Rees 1966), and many superluminal jets have been discovered since then (Vermeulen & Cohen 1994; Britzen et al. 1999). These superluminal motions are typically a few times the speed of light, but would appear larger in the image plane because of magnification; in extreme high-magnification cases speeds up to  $100 c$  would in principle be observable (Hogg & Blandford 1994). The nearly seven-year span of our observations of B1030+074 gives us a good opportunity to investigate the existence of any superluminal movement of the jet in a lens system (see Fig. 8). Second, any components found in both A and B

give extra information to constrain the mass model. The A image in the B1030+074 lens system has a very significant jet while the jet is not resolved in the B image.

Maps of image A at all four epochs, made using the same CLEAN restoring beam, are shown in Fig. 8. At each epoch the jet exhibits a number of knots. Although there are always ambiguities in identifying such jet components from epoch to epoch, the most conservative correspondence is shown by the dotted lines in Fig. 8. There is a suggestion of outward motion of the outermost jet knot 3; the fitted slope implies a proper motion of about  $0.34 \pm 0.20 \text{ mas yr}^{-1}$ , corresponding to a velocity of the jet component in the image plane of about  $7.2 \pm 4.2 c$ . The fitted magnification of the A image for an SIE model is about  $\mu \simeq 3.0$  in the direction along the jet, so in the source plane the jet proper motion is about  $3.0 \pm 1.7 c$ . From top to bottom, the other two jet components give proper motions in the source plane of  $3.7 \pm 2.8 c$  and  $1.1 \pm 0.9 c$ , respectively. The determination of the true jet proper motion relies on the magnification factor which is model dependent. The cusp model can give a range of A image magnification from 3.0 to 5.0. With the  $S_A/S_C \sim 1000$  non-detection constraint the fitted cusped model gives a typical A image magnification of about 2.8, and 3.1 with a  $2.5 \times 10^8 M_\odot$  black hole estimated from the  $M_{BH} - \sigma$  relation. A larger magnification of image A could be achieved if we add a bigger black hole mass to suppress the central image.

The jet in the B image is not resolved. Using the components of the observed A jet from the VLBI/HSA image together with the fitted lens model, we simulated the structure of the B jet using a point spread function (PSF) similar to the restoring beam in our VLBI images (Fig. 9). The simulation confirms that we would not expect to resolve the B jet structure using our current observations.

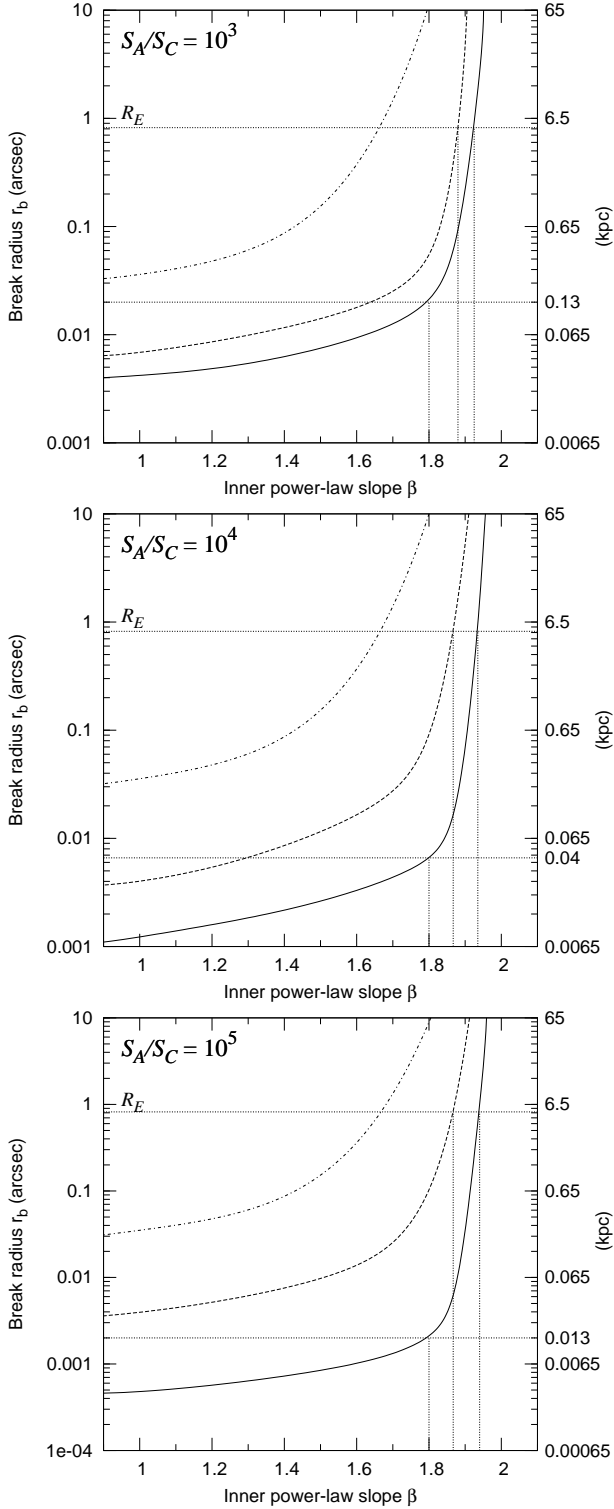


**Figure 7.** Third image detection regions in break radius - inner power-law slope diagram. From the top to the middle and the bottom, the three figures are calculated with primary/central image magnification ratios of  $10^3$ ,  $10^4$  and  $10^5$  respectively. The solid lines are the results calculated by the cusped model, the dashed lines are the results calculated by the cusped model with a  $2.5 \times 10^8 M_\odot$  black hole, the dot-dashed lines are the results calculated by the cusped model with a  $2.5 \times 10^9 M_\odot$  black hole.  $R_E$  is the major axis from a fitted SIE model.

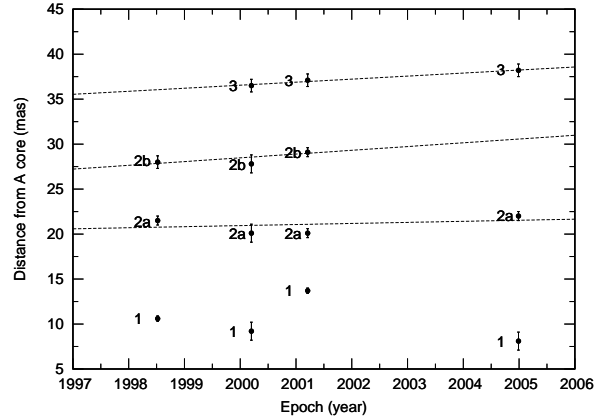
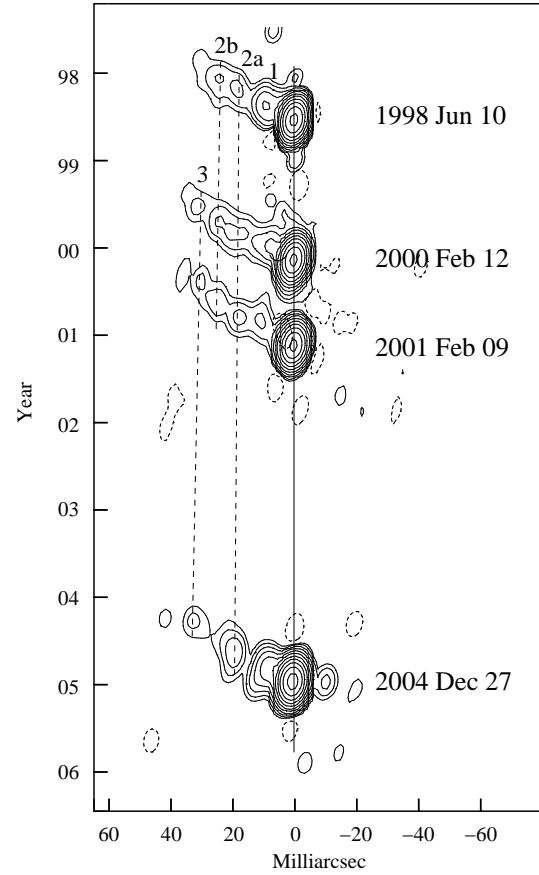


**Figure 8.** Jet proper motion of B1030+074 image A. The top figure shows the most likely correspondence of outgoing individual jet components. All images are restored with the same restoring beam and aligned assuming a stationary core position where the vertical scale is proportional to the time intervals between the different observations. The bottom figure shows the distances between jet components and the core at a position angle of  $60^\circ.1$ . The labelled numbers show the correspondence of jet components. The three dashed lines indicate the results from weighted fits to proper motions of the jet components (2a, 2b, 3), corresponding to the three dashed outlines in the top figure. Fitted slopes are  $0.34 \pm 0.20 \text{ mas yr}^{-1}$  for component 3 ( $\chi^2 = 0.07$ ),  $0.42 \pm 0.32 \text{ mas yr}^{-1}$  for component 2a ( $\chi^2 = 0.7$ ) and  $0.12 \pm 0.11 \text{ mas yr}^{-1}$  ( $\chi^2 = 7.6$ ) for component 2b.

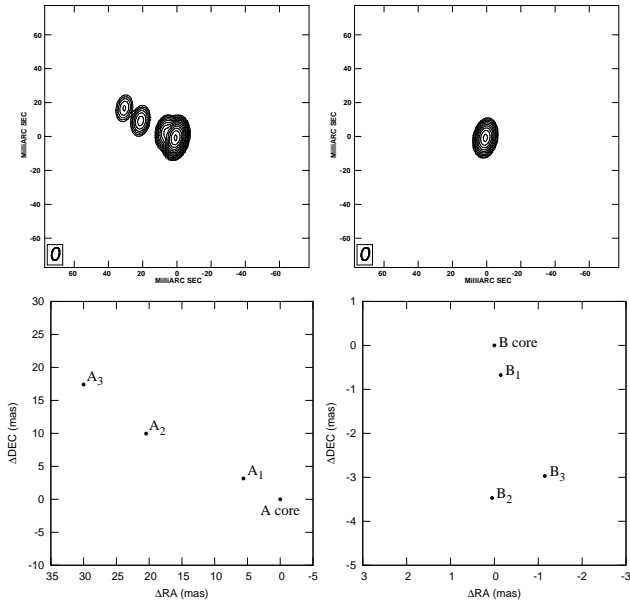


**Figure 9.** Simulated images from the fitted SIE model. They are convolved with a restoring beam of  $7.7 \times 4.5 \text{ mas}^2$  at a position angle of  $-10^\circ.85$ . The contour levels here are the same as Fig. 1. The jet structure in image A is detectable while image B still looks point-like.

## 6 CONCLUSIONS

We have presented a new HSA 1.7-GHz observation of the double-image lens system B1030+074 which was aimed at finding a third image to help to understand the central mass distribution of the lens galaxy. Careful consideration of observational and statistical effects shows that the 90% confidence level of the non-detection in such cases is about 7 times the rms noise (in this case corresponding to  $180 \mu\text{Jy}$ ). This gives a minimum flux ratio of about  $10^3$  between the brightest image and the central image. By comparing with predictions from a cusped model (Muñoz et al. 2001), this non-detection constrains the break radius - inner power-law ( $r_b - \beta$ ) relation, which excludes most of the  $r_b - \beta$  region depicted in Fig. 6 and implies a steep inner power-law slope close to isothermal. Following the  $M_{\text{BH}} - \sigma$  relation (Tremaine et al. 2002), we predicted a central black hole mass of about  $2.5 \times 10^8 M_\odot$ . However, including this black hole mass into the cusped model did not affect the inner power-law slope very much, and would only do so if the black hole mass were increased by a factor 10. The result is consistent with simulations from CDM mass distributions of the lens galaxies (Keeton 2003).

Four-epoch observations gave a possible detection of superluminal motion in the jet. The determination of the true superluminal velocity also depends on the mass model, but with the fitted cusped model, the superluminal motion of the jet is about  $3 c$  in the source plane, although subject to large errors at this stage.

The current 1.7-GHz HSA observation cannot resolve the jet in the B image even with a super-resolved restoring beam. We simulated the B jet from the fitted mass model and convolved it with the restoring beam. This simulated B image still looks like a point source, which is consistent with the observation. A 5-GHz observation may possibly resolve

it if the spectral index is not so steep as to make it below the surface brightness detection limit.

In the next few years, interferometer arrays will come online which should make the detection of central images in gravitational lens systems routine. In particular, the e-MERLIN array will have an L-band sensitivity of  $4.0 \mu\text{Jy beam}^{-1}$  with 12 hours on-source integration. With a resolution of 50 mas at 5 GHz, this instrument is especially well-matched to the problem, since the simpler image structures are more easily mapped with high dynamic range, and the region to be searched to find the central image is at most a few resolution elements. If current theoretical work is correct (e.g. Keeton 2003) this should allow detection of central images, and therefore greatly improved constraints on mass models, in many known radio lens systems.

## Acknowledgements

This work was carried out under financial support from a Marie Curie Research Training Network - Astrophysics Network of Galaxy LEnsing Studies (‘ANGLES’ MRTN-CT-2003-505183). The authors are grateful to Edward Boyce, Shude Mao, John McKean and Roger Barlow for discussions. We also thank the referee Joshua Winn for his constructive comments. The VLA, VLBA and GBT are operated by the National Radio Astronomy Observatory which is a facility of the National Science Foundation operated under cooperative agreement by Associated Universities Inc. The Arecibo Observatory is part of the National Astronomy and Ionosphere Center, which is operated by Cornell University under a cooperative agreement with the National Science Foundation. This research is based in part on observations with the Hubble Space Telescope obtained at the Space Telescope Science Institute, which is operated by Associated Universities for Research in Astronomy for NASA under NASA grant no. NAS5-26555.

## APPENDIX A: ABOUT THE UPPER LIMIT

There are two schools of inferential statistics: frequentist and Bayesian. Each gives different interpretation of probability as well as confidence level. We will investigate two different views on the upper limit.

In the following discussion, we use the following notations: the conditional probability  $P(S|D)$  is for “getting the source, given the data”, and  $P(D|S)$  for “getting the data, given the source”;  $P(D)$  and  $P(S)$  are for data and source probability distributions respectively.

Our specification of the upper limit with desired confidence level is directly from the standard *Neyman construction* (Neyman 1937). To set an upper limit on our non-detection, we simulated the input with artificial sources and analysed the output from our mapping procedure.

Our test is based on several factors:

- ◊ The noise in a CLEANED map is not an objective statistic. Though we can manage to CLEAN it down to thermal noise, it is pointless if the expected weak source is CLEANed out.

- ◊ The recovery of an injected artificial source is stationary and related to its input position and strength, i.e., if we repeat trials with the same input position and strength, the

recovery of the artificial source through the same mapping procedure is same, either false dismissal or not.

◊ The higher the input strength, the better recovery we get, while the lower the input strength the worse recovery. For a source above  $250 \mu\text{Jy}$ , the recovery is almost certain though it will definitely suffer a lossy CLEANing; below  $100 \mu\text{Jy}$ , the recovery is hardly distinguishable from noise.

◊ The background noise of a CLEANed map is non-Gaussian. In sidelobe contaminated region, it is rather obvious. To be unbiased, the recovery test should be in the predicted central image region. We must compromise since we need equal treatment (CLEAN them simultaneously) for both the central image and the artificial sources. We chose the region close to the central image region to minimise this position dependency effect. To avoid confusion with false alarms, we should avoid inject artificial sources on noise spikes. This is easy to check without artificial source injection, and for the small sample test the false alarms are negligible. For example, for Gaussian noise, if you inspect 20000 beams, you will expect one  $4\sigma$  noise spike.

◊ There is no strict constraint on the expected central image flux density distribution unless it violates the flux ratios allowed by the cusped lens model, i.e., the central image should be less bright than the saddle point image B ( $S_C < S_B$ ). Of course, we need to be objective since we can always resort to more complicated models if something odd happens.

◊ A null hypothesis. Since we found no prominent image in the central image region and there is no way to tell it apart from noise spikes even if it is present, we claim non-detection of the central image in our observation. We wish to derive an upper limit on the source strength.

◊ A suboptimal strategy. The optimal statistic could be derived according to the *Neyman-Pearson criterion* if we know the accurate mathematical model of the noise of CLEAN (Allen et al. 2002). However, in the absence of any noise analysis of the CLEAN procedure itself (Cornwell et al. 1999), we conservatively choose the maximum statistic (noise peak) from the central image region in the recovery test as our suboptimal statistic, accompanied by our null hypothesis. This statistic is taken as the counting threshold in our recovery test.

Since we found from our “ring test” that false dismissals happened with artificial sources less than  $200 \mu\text{Jy}$ , we injected 20 artificial sources of  $180 \mu\text{Jy}$  with varying positions close to the central image region and did the recovery test. Most of them are recovered with flux losses of  $\sim 20\text{-}30\%$ , but two of them are recovered with maximum fluxes lower than the  $42 \mu\text{Jy}$  noise peak we obtained from the central image region.

#### (i) Frequentist upper limit:

This is an “objective” approach which is mainly based on the counting frequency in our test. In fact, the standard *Neyman construction* is a frequentist method. This method has been extensively used in weak detection experiments in particle physics and gravitational wave physics (Barlow 2003; Cranmer 2003; Abbott et al. 2004).

Let  $D$  be the detection statistic, and  $D_0$  the suboptimal statistic of a targeted search in our test. If we inject artificial sources greater than or equal to  $S_0$  in the recovery test and

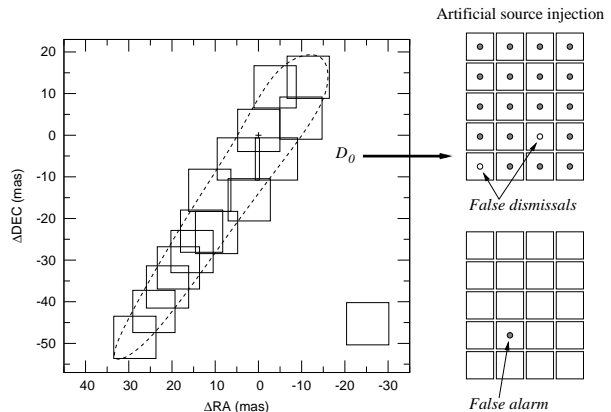


**Figure A1.** Central image CLEANing and artificial source recovery counting. The central image region is covered by  $10 \times 10 \text{ mas}^2$  CLEAN boxes. The statistics  $D_0$  obtained from imaging is used as the counting threshold. The right panel shows the possible false dismissals with artificial source injection and false alarms without artificial source injection in the real test.

we get a fraction  $C$  of trials having residuals above  $D_0$ , then we have a frequentist upper limit  $S_0(C)$  on the strength of the targeted source, with confidence level  $C$ . This frequentist confidence level should be calculated from the integrals of the probability distribution function (PDF)  $p(D|S_0)$ :

$$C(S_0) = P(D \geq D_0 | S_0) = \frac{\int_{D_0}^{\infty} p(D|S_0) dD}{\int_0^{\infty} p(D|S_0) dD}. \quad (\text{A1})$$

In our test, we can count how many values of  $D$  are greater than or equal to  $D_0$  and divide it by the total number of  $D$  values. This is illustrated in Fig. A1. Our null and alternative hypotheses are

$$\begin{aligned} H_0 &: D(S) \leq D_0, \\ H_1 &: D(S) > D_0, \end{aligned} \quad (\text{A2})$$

and the false alarm and false dismissal probabilities are

$$\begin{aligned} \alpha(S) &= \int_{x \in H_1} p(x|H_0) dx, \\ \beta(S) &= \int_{x \in H_0} p(x|H_1) dx. \end{aligned} \quad (\text{A3})$$

We denote the detection probability  $\gamma(S) = 1 - \alpha(S) - \beta(S)$ , then the confidence level will be the detection probability at a source strength  $S_0$  in this case

$$C(S_0) = \gamma(S_0) = 1 - \alpha(S_0) - \beta(S_0) \simeq 1 - \beta(S_0). \quad (\text{A4})$$

Since we have 2 of 20 (remember the predicted central image region is of about 20 beams)  $180 \mu\text{Jy}$  artificial sources covered above  $42 \mu\text{Jy}$  in our test, we will therefore say that if the source to be detected is at  $180 \mu\text{Jy}$  level, it should be detected in our map with a flux over  $42 \mu\text{Jy}$ , with a confidence level of  $(20 - 2)/20 = 90\%$ .

We have found from the recovery test that weak sources are more likely to be CLEANed out, while strong sources more unlikely, i.e.,

$$\begin{aligned} P(D \geq D_0 | S < S_0) &< P(D \geq D_0 | S = S_0), \\ P(D \geq D_0 | S > S_0) &> P(D \geq D_0 | S = S_0), \end{aligned} \quad (\text{A5})$$

then according to the *sum rule*

$$\begin{aligned} P(D \geq D_0 | S \leq S_0) &< P(D \geq D_0 | S = S_0), \\ P(D \geq D_0 | S \geq S_0) &> P(D \geq D_0 | S = S_0). \end{aligned} \quad (\text{A6})$$

So if there is a true source of  $180 \mu\text{Jy}$  of higher, the the probability of getting an observation as small as we obtain or smaller is only 10% or less, i.e., to argue that there is a strong source which happens to have a low fluctuation is very implausible. If we deny the existence of a  $\geq 180 \mu\text{Jy}$  source in this data, we will be right at least 90% of the time.

One should be aware that at different targeted source strength, we could get different confidence levels. Moreover, our recovery test could be biased because of the sampling size and position dependency.

(ii) Bayesian (conditionalist) upper limit:

The Bayesian approach has been consistently used in all statistical studies, especially for hypothesis testing of theoretical predictions provided we know the prior probability distributions of certain physical quantities. This “subjective” approach (for informative objective Bayesian interpretations, see Jaynes & Bretthorst 2003) which always needs a prior knowledge of a certain probability distribution, might not always be practical. The Bayesian confidence level (“degree of belief”) of the upper limit is calculated from the posterior probability  $P(S \leq S_0 | D \geq D_0)$ . We can invert the probability  $P(D|S)$  according to *Bayes’ theorem*

$$\begin{aligned} P(S \leq S_0 | D \geq D_0) &= \frac{P(D \geq D_0 | S \leq S_0)P(S \leq S_0)}{P(D \geq D_0)} \\ &= \frac{\int_0^{S_0} p(S|D \geq D_0) dS}{\int_0^\infty p(S|D \geq D_0) dS} \\ &= \frac{\int_0^{S_0} p(D \geq D_0 | S) p(S) dS}{\int_0^\infty p(D \geq D_0 | S) p(S) dS}. \end{aligned} \quad (\text{A7})$$

Now to calculate the posterior probability  $P(S \leq S_0 | D \geq D_0)$ , we need knowledge about the probability distributions  $P(S \leq S_0)$  and  $P(D \geq D_0)$ . However, the probability distribution of real source strength  $p(S)$  is not known to us. Naturally we could assume a uniform (improper) prior here  $p(S) = \text{constant}$ . Even though we do not have much information about the data bias due to CLEANING, we can integrate the *total probability* of  $P(D)$  decomposed by the “cause” probability  $p(S)$ , see Eq. A7. After normalisation, the probability  $P(S \leq S_0 | D \geq D_0)$  calculation becomes the probability  $P(D \geq D_0 | S \leq S_0)$  calculation, i.e., counting the number of recoveries in the recovery test. Indeed, this uniformly most powerful (UMP) test does exist if we assume a bound  $S$  range, i.e., the integration  $p(D|S)$  over  $(0, \infty)$  converges (for more description of tests in absence of a prior distribution, see Selin 1966). However, the Bayesian confidence level from the UMP test will be very different from the frequentist one. Furthermore, the truth is that the unknown prior source strength distribution we assumed will affect the confidence level determination significantly. Since we have explored from our recovery test that at higher flux density level the recovery probability is higher,

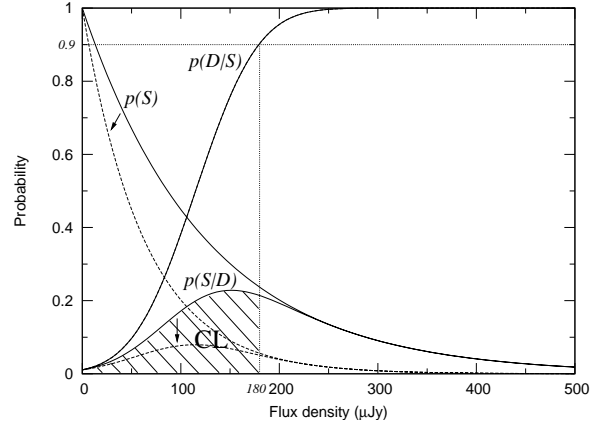


**Figure A2.** Bayesian upper limit. The solid curves present the prior  $p(S)$ , likelihood  $p(D|S)$  and the posterior probability  $p(S|D)$ ; the dashed curves present another case of different prior and consequently different posterior probability of which the confidence level CL increases.

at lower flux density level the recovery probability is lower, we assume a monotonic continuous PDF of  $p(D|S)$  which is illustrated in Fig. A2. We can see from Fig. A2 and Eq. A7 that the probability density  $p(S|D)$  is totally dependent on the profile of prior source PDF  $p(S)$ . The unnormalised inverse probability density  $p(S|D)$  is the product of  $p(D|S)$  and  $p(S)$ . So the Bayesian confidence level of the upper limit will be the fraction of the shaded part in the whole region below the curve, i.e., the cumulative probability  $P(S \leq S_0 | D \geq D_0)$ . In the illustrated case, the confidence level is definitely less than 90%. Obviously, we can manipulate the shape of  $p(S)$  to make the confidence level arbitrary.

In brief, if we want to set up an “objective” upper limit from an experiment, without assuming a Bayesian prior, we should subscribe to the frequentist point of view. The approach taken in our paper is indeed a frequentist approach.

## REFERENCES

- Abbott B. et al., 2004, *Phys. Rev. D*, 69, 082004  
 Allen B., Papa M. A., Schutz B. F., 2002, *Phys. Rev. D*, 66, 102003  
 Barlow R., 2003, in *Statistical Problems in Particle Physics, Astrophysics, and Cosmology*, Lyons L., Mount R., Reitmeyer R., eds., pp. 8–11  
 Boyce E. R., Winn J. N., Hewitt J. N., Myers S. T., 2006, *ApJ*, 648, 73  
 Britzen S., Vermeulen R. C., Taylor G. B., Readhead C. S., Pearson T. J., Henstock D. R., Wilkinson P. N., 1999, in *ASP Conf. Ser. 159: BL Lac Phenomenon*, Takalo L. O. Sillanpää A., eds., pp. 431–+  
 Browne I. W. A. et al., 2003, *MNRAS*, 341, 13  
 Browne I. W. A., Wilkinson P. N., Patnaik A. R., Wrobel J. M., 1998, *MNRAS*, 293, 257  
 Chae K.-H., 2002, *ApJ*, 568, 500  
 Chae K.-H., Khersonsky V. K., Turnshek D. A., 1998, *ApJ*, 506, 80  
 Chen G. H. Hewitt J. N., 1993, *AJ*, 106, 1719  
 Clark B. G., 1980, *A&A*, 89, 377  
 Colless M. et al., 2001, *MNRAS*, 328, 1039

- Combes F., 2004, in IAU Symposium, Ryder S., Pisano D., Walker M., Freeman K., eds., pp. 219–+
- Condon J. J., Cotton W. D., Greisen E. W., Yin Q. F., Perley R. A., Taylor G. B., Broderick J. J., 1998, *AJ*, 115, 1693
- Cornwell T., Braun R., Briggs D. S., 1999, in ASP Conf. Ser. 180: Synthesis Imaging in Radio Astronomy II, Taylor G. B., Carilli C. L., Perley R. A., eds., pp. 151–+
- Cranmer K., 2003, in Statistical Problems in Particle Physics, Astrophysics, and Cosmology, Lyons L., Mount R., Reitmeyer R., eds., pp. 261–+
- de Blok W. J. G., McGaugh S. S., Bosma A., Rubin V. C., 2001, *ApJ*, 552, L23
- Doroshkevich A., Tucker D. L., Allam S., Way M. J., 2004, *A&A*, 418, 7
- Egami E., Neugebauer G., Soifer B. T., Matthews K., Ressler M., Becklin E. E., Murphy Jr. T. W., Dale D. A., 2000, *ApJ*, 535, 561
- Evans N. W. Hunter C., 2002, *ApJ*, 575, 68
- Evans N. W. Wilkinson M. I., 1998, *MNRAS*, 296, 800
- Faber S. M. et al., 1997, *AJ*, 114, 1771
- Fassnacht C. D. et al., 1999, *AJ*, 117, 658
- Ferrarese L. Merritt D., 2000, *ApJ*, 539, L9
- Gebhardt K. et al., 2000, *ApJ*, 539, L13
- Ghez A. M., Salim S., Hornstein S. D., Tanner A., Lu J. R., Morris M., Becklin E. E., Duchêne G., 2005, *ApJ*, 620, 744
- Ghigna S., Moore B., Governato F., Lake G., Quinn T., Stadel J., 2000, *ApJ*, 544, 616
- Gnedin O. Y., Kravtsov A. V., Klypin A. A., Nagai D., 2004, *ApJ*, 616, 16
- Gottlieb D. H., 1994, *Journal of Mathematical Physics*, 35, 5507
- Harvanek M., Stocke J. T., Morse J. A., Rhee G., 1997, *AJ*, 114, 2240
- Högbom J. A., 1974, *A&AS*, 15, 417
- Hogg D. W. Blandford R. D., 1994, *MNRAS*, 268, 889
- Ibata R. A., Lewis G. F., Irwin M. J., Lehár J., Totten E. J., 1999, *AJ*, 118, 1922
- Inada N. et al., 2005, *PASJ*, 57, L7
- Jaynes E. T. Bretthorst G. L., 2003, *Probability Theory: The Logic of Science*. Cambridge, UK: Cambridge University Press, 2003.
- Kang X., Jing Y. P., Mo H. J., Börner G., 2005, *ApJ*, 631, 21
- Keeton C. R., 2001, *ApJ*, 561, 46
- , 2003, *ApJ*, 582, 17
- Koopmans L. V. E., Treu T., Bolton A. S., Burles S., Moustakas L. A., 2006, *ApJ*, 649, 599
- Kormendy J. et al., 1996, *ApJ*, 473, L91+
- Lauer T. R., 1985, *ApJ*, 292, 104
- Lauer T. R. et al., 1997, in ASP Conf. Ser. 116: The Nature of Elliptical Galaxies; 2nd Stromlo Symposium, Arnaboldi M., Da Costa G. S., Saha P., eds., pp. 113–+
- Lewis G. F., Carilli C., Papadopoulos P., Ivison R. J., 2002, *MNRAS*, 330, L15
- Macciò A. V., Moore B., Stadel J., Diemand J., 2006, *MNRAS*, 366, 1529
- Mao S., Witt H. J., Koopmans L. V. E., 2001, *MNRAS*, 323, 301
- McKean J. P. et al., 2005, *MNRAS*, 356, 1009
- McKenzie R. H., 1985, *Journal of Mathematical Physics*, 26, 1592
- Miyoshi M., Moran J., Herrnstein J., Greenhill L., Nakai N., Diamond P., Inoue M., 1995, *Nature*, 373, 127
- Muñoz J. A., Kochanek C. S., Keeton C. R., 2001, *ApJ*, 558, 657
- Myers S. T. et al., 2003, *MNRAS*, 341, 1
- Navarro J. F. Benz W., 1991, *ApJ*, 380, 320
- Navarro J. F., Frenk C. S., White S. D. M., 1996, *ApJ*, 462, 563
- , 1997, *ApJ*, 490, 493
- Neyman J., 1937, *Royal Society of London Philosophical Transactions Series A*, 236, 333
- Peacock J. A., 2003, in AIP Conf. Proc. 666: The Emergence of Cosmic Structure, Holt S. H. Reynolds C. S., eds., pp. 275–290
- Rees M. J., 1966, *Nature*, 211, 468
- Rees M. J. Ostriker J. P., 1977, *MNRAS*, 179, 541
- Robertson B., Yoshida N., Springel V., Hernquist L., 2004, *ApJ*, 606, 32
- Rusin D., Kochanek C. S., Keeton C. R., 2003, *ApJ*, 595, 29
- Rusin D. Ma C.-P., 2001, *ApJ*, 549, L33
- Selin I., 1966, *Detection Theory*. Princeton, New Jersey: Princeton University Press, 1966.
- Sommer-Larsen J., Götz M., Portinari L., 2003, *ApJ*, 596, 47
- Tremaine S. et al., 2002, *ApJ*, 574, 740
- Vermeulen R. C. Cohen M. H., 1994, *ApJ*, 430, 467
- Wallington S. Narayan R., 1993, *ApJ*, 403, 517
- White S. D. M. Frenk C. S., 1991, *ApJ*, 379, 52
- Winn J. N. et al., 2004a, *AJ*, 128, 2696
- Winn J. N., Rusin D., Kochanek C. S., 2003, *ApJ*, 587, 80
- , 2004b, *Nature*, 427, 613
- Xanthopoulos E. et al., 1998, *MNRAS*, 300, 649
- , 2001, in ASP Conf. Ser. 237: Gravitational Lensing: Recent Progress and Future Go, Brainerd T. G. Kochanek C. S., eds., pp. 109–+
- Xanthopoulos E., Browne I. W. A., Wilkinson P. N., Patnaik A. R., 2000, in IAU Symposium